Elastoplastic Inverse Opals as Power-Free Mechanochromic Sensors for Force Recording

*Younghyun Cho, Su Yeon Lee, Lindsay Ellerthorpe, Gang Feng, Gaojian Lin, Gaoxiang Wu, Jie Yin, and Shu Yang**

Light-weight, power-free mechanochromic sensors that can change and record the reflective color depending on the magnitude and rate of the applied force are fabricated from inverse opals by infiltrating the colloidal crystals of silica particles with uncrosslinked SU-8, followed by removal of the colloidal templates. The mechanical sensing range of the materials is high, 17.6–20.4 MPa. Due to elastoplastic deformation of the SU-8 films, the deformed structures and thus colors can be locked after the removal of the load, therefore establishing a quantitative relationship between the mechanical force and optical responses. In comparison, mechanochromic photonic gels reported in the literature typically detect force in the range of 10–100 kPa; once the load is removed, the structure and color return back to the original ones. The mechanochromic sensors are highly sensitive: the ratio of shift in the stopband wavelength to the change in applied strain is up to 5.7 nm per percent, the highest among literature. Comparison of finite element simulations with experiments confirms the elastoplastic deformation of the films and highlights that reconfiguration of pore shape under compression plays a key role in the mechanochromic response.

1. Introduction

Blast-induced traumatic brain injury (TBI) has been the "signature wound" of soldiers who are exposed to blast shockwaves from an explosive device. Little is known about either the potential brain damage or the blast exposure thresholds that induce TBI since soldiers often appear normal with no visible wounds. Repetitive brain injury, however, could lead to temporary loss of memory, reflexes, and judgment, and even long-term effects. Athletes and even normal people could sustain a concussion or TBI as a result of exposure to a certain type of mechanical force in sports or in accidents. The Centers for Disease Control estimates that athletes suffer from roughly 300 000 concussions every year in the US.[1] There have been pressure sensors developed for TBI detection based on optical or electrical signals.[2] They are expensive, cumbersome, and often require power to operate and off-site analysis, thus, time consuming. Further, shockwave detected by these sensors is typically in the range of 10–100 kPa. For an average-size National Football League defensive back (DB), the tackling force is estimated to be 1600 lb by considering the player's mass (≈200 lb) combined with the speed (on average 4.56 s for the 40-yard dash),[3] which corresponds to an impact pressure of ≈6.9 MPa (due to an ≈100 g force) for an object such as a human head and neck (area of ≈20 inch^2). It would be ideal if we could develop a power-free, light-weight, wearable patch that can change color immediately for real-time diagnosis of an approximately MPa impact pressure exposed to an individual and at MHz frequency. By identifying the specific color change in patches worn by soldiers or athletes, a field medic can diagnose instantly the level of shockwave or impact and make decisions whether the soldier or player can return to the field, minimizing the potential of repeated brain injuries.

Previously, we have demonstrated proof-of-concept of color changing TBI dosimeters from holographically patterned, 3D photonic crystals.[4] Photonic crystals are periodic dielectric structures exhibiting a photonic stopband that reflects light in a certain range of wavelength.[5] As beautifully illustrated in butterfly wings, beetle scales, and opals,[6] the structural color originated from scattering on the photonic crystals is much brighter than pigment, and will not fade away nor require power to operate. When exposed to a high-energy shockwave, the microstructures are broken apart preferentially in the weakly connected cleavage planes, resulting in color degradation or lost it all. Recently, there are increasing interests in mechanochromic effects in photonic gels (see ref.[7], which change color due to elastic deformation of soft gels under a load, typically in the range of 10–100 kPa. However, upon removal of the force, the color returns back to the original state. Therefore, questions remain as whether we can quantify the structural deformation

Dr. Y. Cho, Dr. S. Y. Lee, G. Wu, Prof. S. Yang
Department of Materials Science and Engineering
University of Pennsylvania
3231 Walnut Street, Philadelphia, PA 19104, USA
E-mail: shuyang@seas.upenn.edu
L. Ellerthorpe, Prof. G. Feng
Department of Mechanical Engineering
Villanova University
Villanova, PA 19085, USA
G. Lin, Prof. J. Yin
Department of Mechanical Engineering
Temple University
Philadelphia, PA 19122, USA

DOI: 10.1002/adfm.201502774

versus color appearance versus the level of exposed mechanical force or pressure. Can the crystal record different levels of the force via color change even after removal of the force? How to mass-produce such color changing patches over a large area?

Here, we fabricated inverse opals by infiltrating the colloidal crystals of silica particles (diameters of 320, 285, and 238 nm) with uncrosslinked thermoplastic polymer SU-8, followed by removal of the silica colloidal templates.[8] The prepared films showed mechanochromic response, where the degree of color change corresponded to the magnitude and rate of the applied force. Due to elastoplastic deformation of SU-8 films, the deformed structure and thus color were locked after removal of the load, allowing us to establish the quantitative relationship between the mechanical force and optical responses. Because SU-8 is rather stiff, the mechanical sensing range of our materials is high enough (17.6–20.4 MPa) to measure the typical impact loading exposed to a football player. The patches were highly sensitive: $\Delta\lambda/\Delta\varepsilon$, the ratio of shift in the stopband wavelength to the change in applied strain, was up to 5.7 nm/%, the highest value compared to literature ones. To better understand the mechanical deformation mechanism, we carried out finite element simulation of the deformation process, which corroborated well with experiments. It confirmed the elastoplastic deformation of the film and highlighted that reconfiguration of pore shape under compression played a key role in the mechanochromic response.

2. Result and Discussion

Photonic crystals self-assembled from monodispersed colloidal particles are low-cost and their fabrication is scalable to an area over cm^2 by sedimentation,[9] spin coating (e.g., 4 in. wafer size),[10] doctor blade coating in a continuous fashion at a coating speed of 1 mm s^{-1}.[11] The displayed color can be tuned by varying the particle size, lattice spacing, volume filling fraction, and refractive index contrast within the porous network.[12] Meanwhile, through backfilling of monomers, followed by polymerization and etching to remove the colloidal template, many have created polymeric inverse opals (**Figure 1**). They are light weight (≈70% porosity due to the close-packing of the nanoparticle template) and can change colors in responsive to external stimuli,[13] including solvent,[14] pH and ionic strength,[15] temperature,[16] light,[17] magnetic field,[13b] and mechanical compression or stretching.[18] The color exhibited in so-called mechanochromic gels, which are typically made from elastomers, hydrogels, and swellable block copolymers, returns to the original state once the stimulus is removed attributed to the elastic nature of the materials. Therefore, it will be difficult to permanently and accurately record the degree of deformation in mechanochromic gels for later off-site checking. In addition, the force that can be sensed by mechanochromic gels is rather small, 10–100 kPa.

Here, we chose a thermoplastic material, SU-8, with a low glass transition temperature (T_g, 50–60 °C) and a low melting temperature (T_m, 80 °C) to prepare the inverse opals for force sensing. Upon heating to 95 °C, the film begins to flow and its viscosity is significantly lowered to ≈5 Pa s due to its low average molecular weight, ≈1397 g mol^{-1}. Thus it has been used in capillary force lithography to pattern various structures.[19] After infiltration, the SU-8 film is cooled down to room temperature and becomes glassy again. If needed, it can be further photocrosslinked. Compared to conventional glassy polymers, such as polystyrene (PS), its short infiltration time is especially attractive. The filling time by capillary force is given by[20]

$$t = \frac{2\eta_s h^2}{R\gamma\cos\theta} \quad (1)$$

Where η_s is the viscosity of the filling liquid, h is the channel height, R is the hydraulic radius of the channel, γ is the liquid surface tension, and θ is the liquid contact angle at the liquid–channel interface. Accordingly, it takes ≈78 s for SU-8 to completely infiltrate the 3D structures with a thickness of

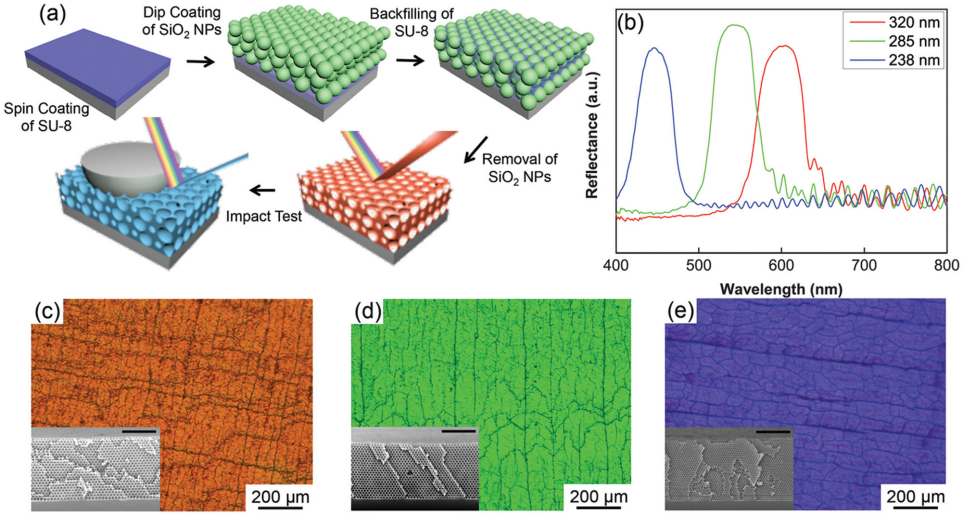

Figure 1. a) Schematic illustration of the process for the preparation of an SU-8 inverse opal. b) Reflectance spectra of the pristine inverse opal structures prepared from different-sized nanoparticles. c–e) Optical microscopy images of various inverse opal structures prepared from silica nanoparticles with diameters of c) 320 nm, d) 285, and e) 238 nm. Inset: Cross-sectional FE-SEM images of each structure. Scale bars in the inset: 3 μm.

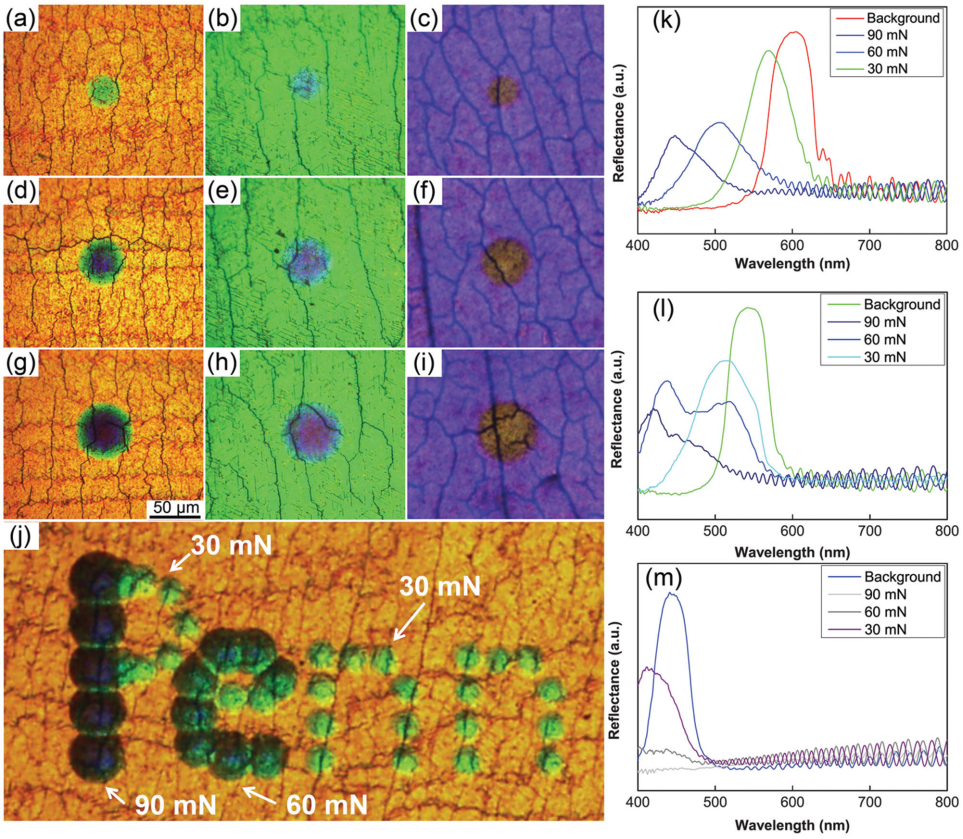

Figure 2. Optical microscopy images of various inverse opal structures with a diameter of a,d,g) 320 nm, b,e,h) 285 nm, and c,f,i) 238 nm after nanoindentation at a,b,c) 30 mN, d,e,f) 60 mN, and g,h,i) 90 mN. j) The letters consisting of three different spots indented at 30, 60, and 90 mN. Reflectance spectra of inverse opal structures after indentation with a particle diameter of k) 320 nm, l) 285 nm, and m) 238 nm. The force was applied by a spherical indenter with a diameter of 301 μm at a fixed loading rate of 100 mN s^{-1}.

10 μm, whereas it will take 1645 days for PS to fill the same structure since the latter has much higher viscosity (≈10^6 Pa s at 100 °C[21], which is five to six orders magnitude higher than that of SU-8. Also PS is more brittle with a higher T_g (≈100 °C) and a higher Young's modulus (≈3 GPa) versus ≈1.2 GPa from uncrosslinked SU-8 (see Figure S1, Supporting Information).[22] Thus, PS film will easily break and form cracks like the crosslinked SU-8 instead of being elastoplastically deformed to record color/force.

Figure 2 shows the optical microscopy images of SU-8 inverse opals after removal of the indentation forces of 30, 60, and 90 mN, respectively. The force was applied by a spherical indenter with a diameter of 301 μm at a fixed loading rate of 100 mN s^{-1}. Before indentation, the pristine SU-8 films templated from silica nanoparticles of diameters 320, 285, and 238 nm showed reflectance peaks at 605, 544, and 446 nm, respectively (Figure 1b). Upon removal of the applied indentation force, all films showed blue shift of the reflectance peaks when increasing the indentation force from 30 to 90 mN (see Figure 2k). For the one obtained from 320 nm diameter particles, the color blueshifted from red (605 nm) to green (570 nm), blue (500 nm), and purple (440 nm). For the inverse opal obtained from 238 nm diameter nanoparticles, the apparent color is already close to the edge of visible wavelength (446 nm). After indentation, the color blue shifted further into UV wavelength (see Figure 2m), which could not be discerned by naked eyes (Figure 2c,f,i). To better illustrate the color correlation to the applied forces, we wrote the word "Penn" from the 320 nm inverse opal with purple (90 mN), blue (60 mN), and green dots (30 mN) in the background of red/orange color (see Figure 2j).

As evidenced by the residual indent in the films after removal of the force (**Figure 3**), the plastic deformation of the structures accounts for the blueshift of the reflectance peaks observed in all the inverse opals after removal of the loading. Generally, the larger the magnitude of the applied force, the deeper is the residual indent and the darker is the color. Another evidence for plastic deformation can be found in the gradient color change from the center to the edge within the indented region (see the dots in Figure 2a,d,g), where the center in the sample undergoes the largest compression due to the spherical shape of the indenter. The observed gradient color change is also a good example for showing the correlation between the plastic strain and color change.

Given the length-scale-dependent elastoplastic behavior observed in highly crosslinked SU-8 microframes,[23] it is challenging to measure the stress–strain behaviors of the inverse opals with nanoscaled constituent.[24] Here, from the microindentation experiments, we obtained some qualitative information on the mechanical response of the inverse opals by measuring the indentation depth and the respective recovered

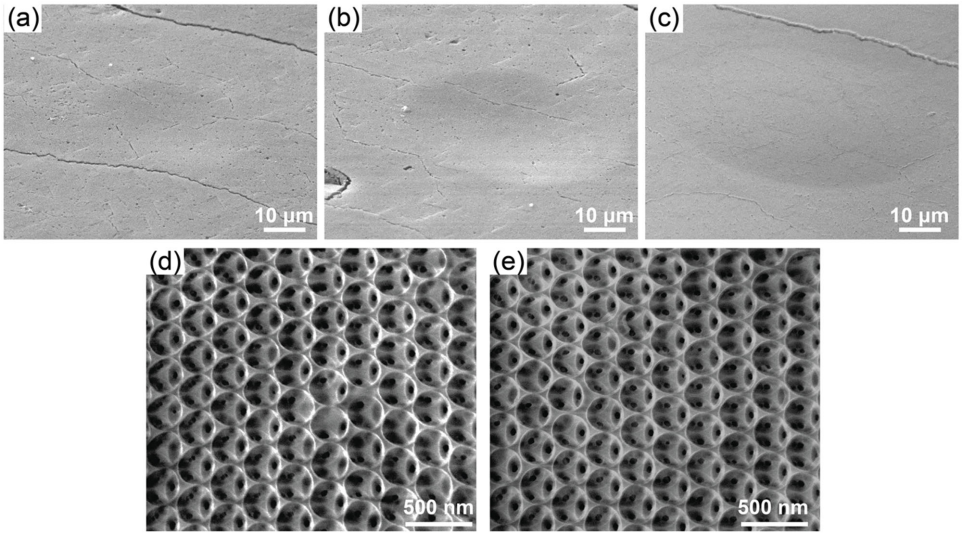

Figure 3. a–c) Low magnification FE-SEM images of the inverse opal structures indented with a load of a) 30 mN, b) 60 mN, and c) 90 mN. d,e) Top-view high-magnification FE-SEM images of the d) pristine and e) indented film with a load of 90 mN.

displacement at the central indented region, which could be approximated as being under uniaxial compression due to the far larger indenter radius than the indentation depth. As seen from Figure S2a (Supporting Information), the increasing recovered thickness with the applied compressive strain implied a plastic strain-hardening behavior, similar to that observed in the cured SU-8 materials.[24]

Compared to the mechanochromic gel sensors reported in the literature,[7] our inverse opals from uncrosslinked SU-8 offer several distinct advantages. (1) Our sensors are load history dependent: different forces (or intrinsic pressures) applied to the structures can be permanently recorded after removal of the force, which is in sharp contrast to the mechanochromic gels reported in the literature.[7] For the latter, it is difficult to record or measure the actual force applied to the photonic crystal or it will need an in situ imaging device to detect the instant optical signal. In the case of uncrosslinked SU-8 inverse opals, above a critical threshold, elastoplastic deformation is induced, leading to permanent deformation. After unloading, the deformed configuration may recover to a small extent, but is locked-in. The applied force can be estimated by multiplying the deformation area and the pressure documented through the signature color. More importantly, the optical response can be recorded and characterized postimpact at anytime. (2) The uncrosslinked SU-8 is glassy with a Young's modulus of ≈1.2 GPa at room temperature, that is ≈10^3 times or more stiffer than the elastomers used in prior mechanochromic gel sensors, which have Young's modulus ranging from a few hundred kPa to a few MPa. For the latter, the force being sensed is rather small (≈10 kPa).[18a,c,e,25] In contrast, an order of magnitude higher loading pressure can be recorded in our SU-8 inverse opal (17.6–20.4 MPa, which was calculated from the applied force divided by contact area obtained from field-emission scanning electron microscopy (FE-SEM) and optical microscopy images), on the same order of or even higher than the tackling force received by an average football player. Importantly, here we used uncrosslinked SU-8, which could undergo large elastoplastic deformation without breaking apart, allowing it to record the force, in sharp contrast to the brittle, crosslinked SU-8 film (Young's modulus ≈2–3 GPa,[26] T_g ≈ 200 °C) or PS. Previously, we show that under blast pressure, the 3D film made from crosslinked SU-8 would crack and fracture, and thus disintegration of the color.[4a] So it is not possible to generate spectra of color correlating to forces of different magnitude.

The original colloids assembled from silica nanoparticles form face-centered cubic (FCC) structures with the (111) plane parallel to the substrate to minimize the total repulsive energy (Figure 1c–e). The stopband peak position (λ) in the [111] direction from the normal incident light is determined by Bragg's law

$$\lambda = 2dn_{\text{eff}} = \left(\frac{8}{3}\right)^{1/2} D(n_p^2\phi + n_m^2(1-\phi))^{1/2} \quad (2)$$

where d is the lattice spacing, n_{eff} is the effective refractive index, D is the particle diameter, is the volume filling fraction of particle in the matrix, and n_p and n_m are the refractive indices of the particles and medium, respectively. According to Equation (2), we could derive the effective nanoparticle diameter for a given reflectance peak of the inverse opal. For example, for a reflectance peak at 605 nm, we obtained the effective particle diameter as 307 nm, in good agreement with the actual particle size (error ≈4%). Likewise, we could obtain the effective pore diameters as 292, 263, and 233 nm from 320 nm diameter inverse opals under normal force of 30, 60, and 90 mN, respectively. **Figure 4** shows the cross-sectional SEM images of the deformed 320 nm inverse opals under various loading forces in the [111] direction (that is, perpendicular to the substrate). In order to observe the internal structure of indented area, the sample was prepared by focused ion beam (FIB) and they were tilted in SEM images. Therefore, pore size was calculated by taking consideration of the tilting angle. To further confirm the pore size, we calculated the ratio of pore size in the vertical direction versus that in the lateral direction and compare it with

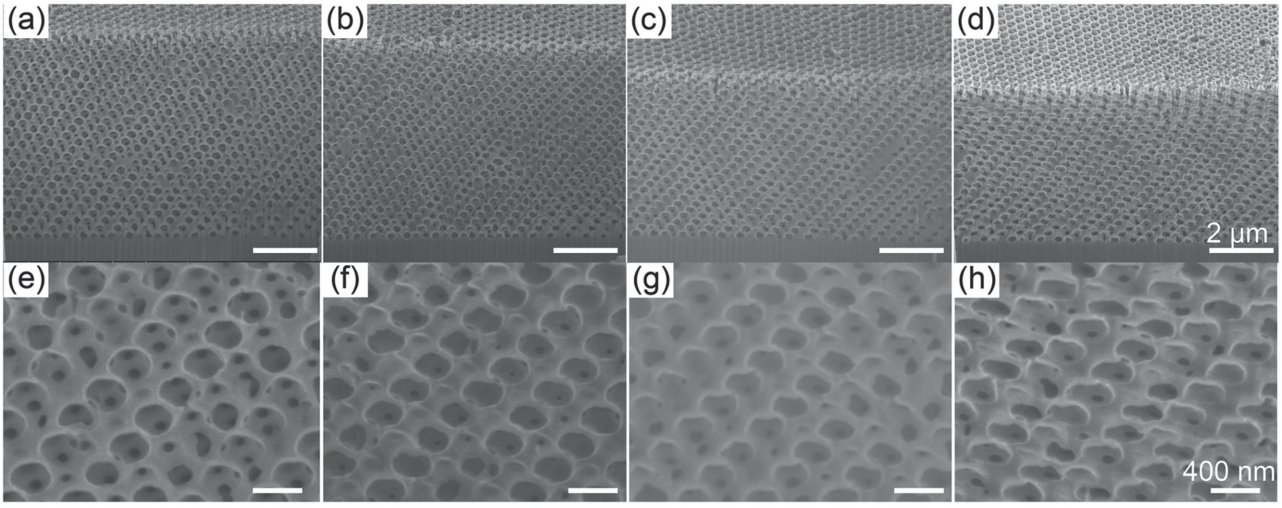

Figure 4. Low- (top panel) and high-(bottom panel) magnification FE-SEM images (cross-sectional view, [111] direction) of the inverse opal structure obtained from particles with a diameter of 320 nm. a,e) Pristine inverse opal, b,f) indented at 30 mN, c,g) indented at 60 mN, and d,h) indented at 90 mN.

reference (actual pore size without indentation). The pore size measured by SEM in the out-of-plane ([111]) direction gradually decreased from 320 nm (pristine sample) to 297, 262, and 227 nm with the increase of the applied force to 30, 60, and 90 mN, respectively, which is in good agreement with the data obtained from reflectance peaks. Notably, the voids in the inverse opals changed shape from spheres to ellipsoids. However, the in-plane lattice spacing and pore shape did not change significantly in the (111) plane under the normal force (Figure 3d,e), indicating that the change in lattice constant mainly occurred uniaxially in the [111] direction.

To record the color change, it is critical to understand the rate-dependent deformation and/or recovery. Depending on the type of injuries, whether it is due to car accident, concussion when playing football, or due to blast injury, the shockwave occurs in the range of nanoseconds to milliseconds.[27] SU-8 materials tested using dynamic mechanical analysis showed rate-dependent viscoelastic characteristics (Figure S1, Supporting Information). The higher frequency represents a larger effective strain rate. The elastic modulus (i.e., storage modulus) drops slightly with the increase of strain rate, whereas the viscous modulus (i.e., loss modulus) decreases with the increase of strain rate when measured at a temperature below T_g, which is room temperature in Figure S1 (Supporting Information). Thus, the constituent SU-8 materials show an elastic viscoplastic behavior with strain-rate stiffening, similar to that of the cured SU-8 microframe structure.[24] For the inverse opal SU-8 nanostructured films, insights on how the strain rate influences its elastoplastic behavior can be obtained from the indentation data shown in Figure S2b (Supporting Information) with characteristic penetration depth as a function of the loading rate, i.e., a slower loading rate leads to a deeper penetration. Exactly how the strain rate influences the yield stress and strain hardening behavior is beyond the scope of this paper. We will explore it in the future.

As seen in **Figure 5**, at a fixed load of 30 mN, the reflectance spectra blueshifted when lowering the loading rate. This can be explained as follows. At a lower strain rate, a higher viscous modulus and viscoplastic behavior are more dominant than the elastic behavior, and thus resulting in a deeper indentation depth and smaller recovery ratio. When strain rate increases, the elastic deformation becomes increasingly significant and thus shallower indentation and larger recovery ratio. Supporting this, the indentation depth at 0.1 mN s^{-1} was the largest (2170 nm) compared to 1830 nm for 1 mN s^{-1} and 1660 nm for 10 mN s^{-1}. Correspondingly, only 8% of the indentation depth was recovered from the film indented at 0.1 mN s^{-1} after the load

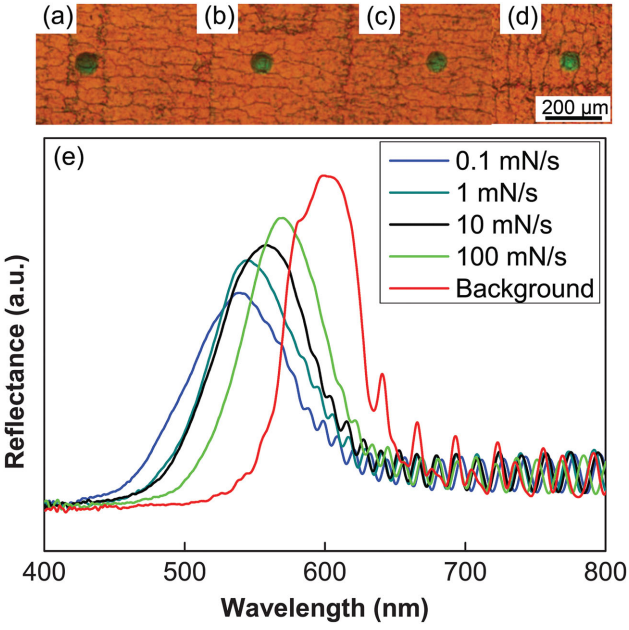

Figure 5. Optical microscopy images of inverse opal structures with a diameter of 320 nm indented at a loading rate of a) 0.1 mN s^{-1}, b) 1 mN s^{-1}, c) 10 mN s^{-1}, and d) 100 mN s^{-1}. The load is fixed at 30 mN for all the samples. e) Reflectance spectra of inverse opal structures after indentation.

was removed versus 26% and 29% when indented at 1 mN s^{-1} and 10 mN s^{-1}, respectively (Figure S2, Supporting Information). As a result, they show different degrees of stopband shift. In practice, after a patch experiences an impact, we may want to determine both the impact pressure and impact rate. Figures 2 and 5 indicate that the color change due to an impact would be dominated by the magnitude of the impact pressure. Therefore, by examining the color change in the impact imprint, we should be able to estimate the impact pressure. The impact load can then be determined by multiplying the impact pressure and the impact imprint area. Further, Figure 5 and Figure S2 (Supporting Information) imply that the impact rate could be determined by analyzing both the color change and the shape of the residual impact morphology, particularly the depth/area and the aspect ratio of the impact-induced permanent imprint. The deconvolution of the impact load and loading rate would be investigated in future work.

To quantify the mechanochromic sensitivity of our films, we calculate the $\Delta\lambda/\Delta\varepsilon$ in comparison to literature values.[7] $\Delta\lambda/\Delta\varepsilon$ is defined as the shift in the stopband wavelength versus the change in applied strain, typically from uniaxial compression or tension. The mechanochromic sensor with a high sensitivity value can show a significant color change even at a small change of strain. In our system, the sample thickness is ≈10 μm, and the indentation depth ranges from 1.75–4.5 μm. For a large indenter with a radius of 150 μm, the indentation on the centered region could be approximate as uniaxial compression. As seen from Figure 4, there was uniform topography of compression from right below the indented region to the film–substrate interface. By measuring the thickness change under the indentation center from SEM images, we calculate $\Delta\varepsilon$ as equivalent uniaxial compressive strain. The mechanochromic sensitivity from the 320 nm inverse opal is estimated as 5.7 nm/%, the highest so far in comparison with the literature (see Figure S3, Supporting Information).[7] We note that if we use the applied strain calculated from indentation, $\Delta\lambda/\Delta\varepsilon$ would have been even higher.

To reveal the underlying deformation mechanism as well as provide further insights into the mechanical responses under different loads, we carried out micromechanical modeling using the finite element method (FEM) (see **Figure 6**) based on the deduced approximate data from the nanoindentation (see the Supporting Information). A periodic unit cell with the pore size of 320 nm is first studied, assuming plastic deformation under uniaxial compression along the [111] direction, i.e. Z-axis, where the loading is transmitted through diagonally connected narrow necking arches, tangential to two pores. Figure 6a shows the von Mises stress contour of the unit cell under a compressed strain of about 0.1. It shows that due to the heterogeneous cross-section shape, the stress is highly concentrated and localized in the diagonal necking regions (highlighted in red), whereas the pillars (highlighted in blue) connecting the necking regions undergo much smaller deformation with its principal stress over 50 times lower than that in the necking area. Figure 6b shows the equivalent plastic strain contour of the unit cell of the inverse opal FCC structure. It shows that the highly stress-concentrated regions correspond to the locations with large plastic deformation as highlighted in red, whereas the pillars are under slight compression with negligible plastic deformation as highlighted in blue. When indented by a large spherical tip, the circular pores in the (111) plane are homogeneously stretched in all directions, and thus maintaining their circular shapes (Figure 6c and Figure 3d,e). However, the necking arches in the cross-sectional plane (Z-axis) are bent and sheared to accommodate the large compression, and thus the pores transform from spheres to ellipsoids (Figure 6d),

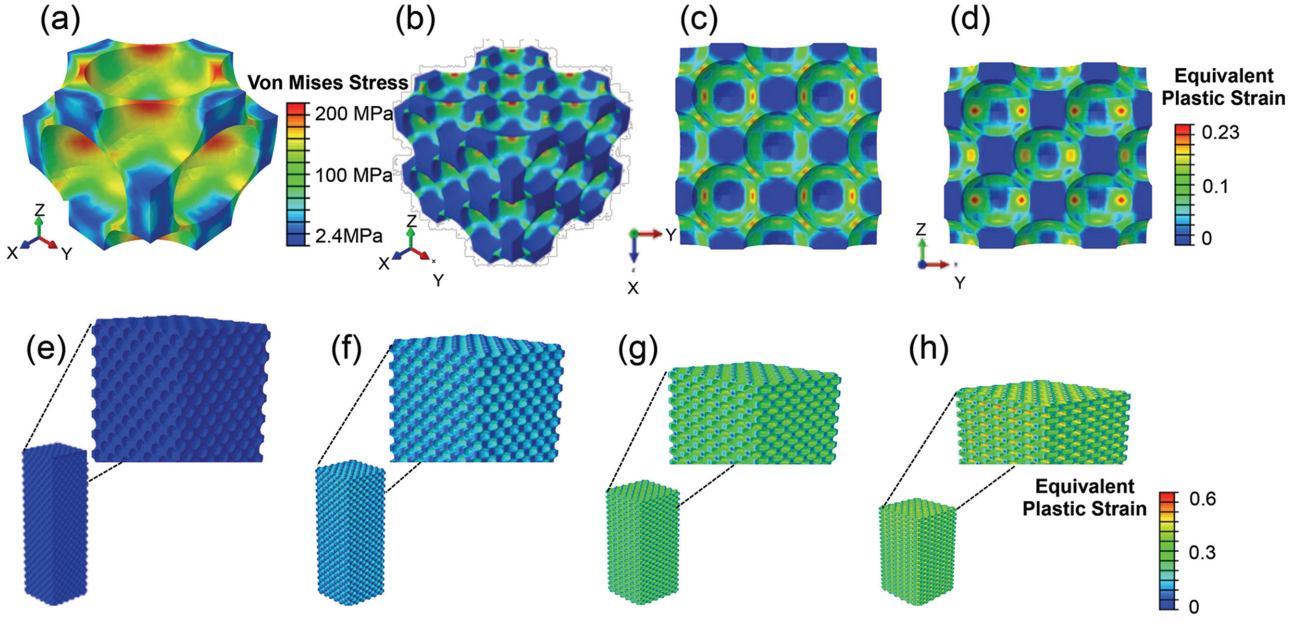

Figure 6. 3D FEM simulation results on the deformation of a–d) a periodic unit cell under uniaxial compression and e–h) overall deformation of the inverse opal structures under different loads. a) von Mises stress contour of a unit cell, b) the equivalent plastic strain contour of a unit cell, c) top view, and d) side view. e–h) 3D geometry of the simulated structure model under different load. e) Before indentation and f–h) permanently deformed structures after loading and unloading with a load of f) 30 mN, g) 60 mN, and h) 90 mN. Insets are high resolutions of the deformed configuration.

in agreement with experiments shown in Figure 4. After unloading, the highly stress-concentrated local regions cannot recover back to the original state despite the large recovery in the pillars, which is attributed to the elastoplastic deformation in the uncrosslinked SU-8 film below the glass transition temperature. As shown by Singamaneni et al. in pattern transformation of microporous 2D membranes from SU-8,[28] different from elastomeric membranes, the deformation of the porous membrane can occur at a lower critical strain in elastoplastic materials due to lower elastic limit. In turn, the deformed structure can be preserved even after prolonged thermal annealing close to T_g after removal of the stress.

To further investigate the overall mechanical response observed in experiments and elucidate the interplay between layers of the crystal, we simulated the indentation process on the multilayered crystal structure using FEM, where a simplified multilayered model is constructed with 20 layers of unit cells (equivalent thickness of 9.6 μm) with symmetric boundary conditions as shown in Figure 6e (see the Experimental Section and Supporting Information). The same respective indentation depth as the experiments for different loading is applied, which corresponds to an indentation load of 30, 60, and 90 mN. After removal of the loading, the simulation results show good agreement on the recovery ratio for all three loadings (see the Supporting Information). Figure 6f–h show the respective remaining deformed shape corresponding to the case of removal of an indentation load of 30, 60, and 90 mN. The simulation results show that the loading is transmitted through the pillars and interconnecting arches. Unlike the orthogonal arrangement of ellipses in the XY-plane in 2D hexagonal arrays of porous SU-8 films[28,29] or plastic deformation of 3D SU-8 microstructures[24] under compression,[28] where the nodes rotate to release the stress, circular pores in the Z-axis of the inverse opal are deformed into elliptical shapes with similar size throughout the entire film thickness and the short axis aligned uniformly in parallel to the loading direction (Figure S4, Supporting Information). Such axial alignment along the loading direction has been reported in holographically patterned, microstructured SU-8.[24] As the indentation depth increases, the short axis of the pore is further compressed due to the bending of connecting arches accompanied by its long stretched axis due to the lateral expansion of the pillars under compression. As the indentation depth becomes larger the pores become more oblate as shown in Figure 6f–h and there is less thickness recovery, which corroborates very well with experiments.

3. Conclusion

In summary, we have demonstrated light-weight, power-free mechanochromic sensors based on the inverse opals made from elastoplastic, uncrosslinked SU-8. Mechanical deformation has been investigated in elastomeric 3D structures[13a,18a-c,18e,25] and to some extent in highly crosslinked polymeric 3D microstructures.[24,30] However, the former is most suitable to measure small forces or pressure (10–100 kPa) and cannot record the force accurately, while the latter is often cracked or fractured upon deformation, losing the film integrity, and will not allow for accurately discerning the degree of deformation and force. The inverse opals created from the uncrosslinked SU-8 in our system offer several unique features, including (1) they are deformable but maintain the structural integrity after indentation. (2) The deformed structures and colors can be locked-in after deformation, allowing us to create barcode-like patches to correlate the color and mechanical force, and measure rate dependence without the use of power or expensive in situ imaging tools. (3) They offer the highest mechanochromic sensitivity ($\Delta\lambda/\Delta\varepsilon$ = 5.7 nm/%) compared to those reported in the literature so far, yet they are easy to fabricate and detect. (4) Because SU-8 is rather stiff, the mechanical sensing range of our materials is high enough (17.6–20.4 MPa) to measure the typical impact loading exposed to a football player. To better understand the deformation mechanisms, we carried out FEM simulations, which agreed well with the experiments. In particular, FEM highlighted an important feature of our mechanochromic sensor, which is elastoplastic response of the uncrosslinked SU-8 film. The insights presented here can be applied to design and fabricate power-free mechanochromic sensors to detect and record a wide range of impact pressures and rate (up to MHz frequency) by fine-tuning materials of various stiffness and viscoelasticity. We expect that the created patches can be worn on helmets and jackets on multiple locations, allowing for multipoint assessment of the level of shock-waves soldiers or athletes are exposed to. As a consequence, we can provide knowledge for the design of shock-wave absorbers to prevent concussion or TBI.

4. Experimental Section

Synthesis of Silica Nanoparticles: Monodisperse SiO_2 nanoparticles with a diameter of 320, 285, and 238 nm were synthesized by a combination of the two-phase method for the synthesis of seed nanoparticles[31] and the modified Stöber method[31,32] for the growth of nanoparticles with diameter larger than 200 nm.

Preparation of SU-8 Inverse Opals: The literature procedure to prepare the SU-8 inverse opal was followed.[8] First, the negative photoresist SU-8 2 (Microchem Corp.) was spin-coated onto a pre-cleaned silicon wafer to obtain a thickness of 5 μm. Then, the film was soft-baked at 95 °C for 5 min to evaporate the solvent. Oxygen plasma treatment (Plasma Cleaner, Harrick) was performed for 60 s to generate a hydrophilic surface. The film was vertically dipped in an aqueous suspension of monodisperse silica particles (2 wt%) and slowly pulled out at a speed of 0.25–0.80 μm s^{-1} to deposit the colloidal crystals with a controlled thickness. The colloidal crystal of silica particles was back-filled with SU-8 by capillary force at 120 °C for 10 min. SU-8 inverse opal was obtained after etching away silica nanoparticles in a hydrofluoric acid (5 wt%) for 10 min at room temperature.

Impact/Nanoindentation Test: An Agilent Nano Indenter G200 with continuous stiffness measurement capability was used to perform nanoindentation. A sapphire spherical tip with a diameter of 301 μm was utilized. The sample was bonded on an aluminum stub and the sapphire tip indented the sample with different loading rates ranging from 0.1 to 100 mN s^{-1} and at loads of 30, 60, and 90 mN, respectively. The unloading was programmed at 1/4 of the loading rate. For each sample, we indented at least eight places.

Characterization: FE-SEM measurement was carried out using a JEOL 7500F HRSEM to examine the indented surface morphology. In order to observe the internal structure of indented sample, the sample was cut by FIB (FEI Strata DB235 FIB) at an operating voltage and current of 30 kV and 50 pA, respectively. The reflectance of the samples was measured by Filmetrics F40 at a wavelength range of 400–850 nm. In

order to measure the reflectance coming from the indented area not from the background, the smallest beam size (≈10 μm) was used, which is much smaller than the size of the contact area (≈25–50 μm).

FEM Simulations: The mechanical deformation behaviors of the SU-8 inverse opals under different indention depth were simulated using commercial software ABAQUS. The SU-8 inverse opal structures were modeled as an isotropic and linear strain-hardening elastoplastic materials, respectively, depending on their stress–strain relationship.[22] To explore the deformation mechanism, a 3D periodic unit cell with size of 470 × 470 × 470 nm was simulated under uniaxial compression with imposed periodic boundary conditions. The 3D microstructure constructed by 12(W) × 12(L) × 20(H) unit cells was indented in the center by a rigid and frictionless spherical indenter modeled as a rigid body in hard contact. The indentation loading and unloading process were controlled through the displacement of rigid indenter. Due to the symmetry of the structure, for simplification only one-quarter of the whole structure was modeled with symmetric boundary conditions and the sample bottom was fixed. To reveal the underlying deformation mechanism under indentation, a representative unit cell with periodic boundary condition is simulated under uniaxial compression. The dimension of unit cell is 470 nm × 470 nm × 470 nm, which is meshed to 7187 C3D4 elements. A displacement of 0.1 mm is applied to compress the unit cell. To simulate the overall mechanical deformation of the inverse opal structures under indentation, a simplified 3D model is constructed with the same height as the sample in experiment. Theoretically, an indentation depth of over 1 mm will laterally indent more than 100 units in the sample, which makes it impossible to simulate the real condition of the experiments using FEM simulation. A simplified 3D model is constructed with a small region of a lateral dimension of 2.82 μm × 2.82 μm but with the same sample height to capture the overall mechanical deformation and shape changes of pores under indentation. One quarter of the microstructure is modeled with symmetric boundary condition and it has a total number 447 120 C3D4 elements. The rigid spherical indentor is modeled as a rigid body and the indentation is controlled through displacement. The indentation displacement is set to be the same as experiments, where the 3D microstructure is indented with a penetration depth of 1750, 3275, and 4535 nm, corresponding to the respective indentation force of 30, 60, and 90 mN, respectively. The stress–strain curve of the materials is assumed to be a linear elastoplastic. The simulated recovery ratio of the whole structures shows good agreements with the experimental measurements (Table S1, Supporting Information).

Supporting Information

Supporting Information is available from the Wiley Online Library or from the author.

Acknowledgements

Y.C. and S.Y.L. contributed equally to this work. This work was supported by Berkman Opportunity Fund. The University of Pennsylvania National Science Foundation (NSF) MRSEC grant (DMR-1120901) and Nanoscale Characterization Facility (NCF) are acknowledged for access to SEM.

Received: July 7, 2015
Revised: July 25, 2015
Published online: August 26, 2015

[1] *MMWR Morb Mortal Wkly Rep.*, Vol. 46, Centers for Disease Control and Prevention (CDC), GA, USA **1997**, p. 224.
[2] a) K. S. Budil, D. M. Gold, K. G. Estabrook, B. A. Remington, J. Kane, P. M. Bell, D. Pennington, C. Brown, S. Hatchett, J. A. Koch, M. H. Key, M. D. Perry, *Rev. Sci. Instrum.* **1999**, *70*, 806; b) Y.-C. Chao, W.-J. Lai, C.-Y. Chen, H.-F. Meng, H.-W. Zan, S.-F. Horng, *Appl. Phys. Lett.* **2009**, *95*, 253306; c) M. Chavko, W. A. Koller, W. K. Prusaczyk, R. M. McCarron, *J. Neurosci. Methods* **2007**, *159*, 277; d) N. Wu, W. H. Wang, Y. Tian, X. T. Zou, M. Maffeo, C. Niezrecki, J. L. Chen, X. W. Wang, *Opt. Express* **2011**, *19*, 10797; e) N. Wu, X. T. Zou, Y. Tian, J. Fitek, M. Maffeo, C. Niezrecki, J. Chen, X. W. Wang, *Meas. Sci. Technol.* **2012**, *23*, 7; f) X. T. Zou, N. Wu, Y. Tian, C. Niezrecki, J. L. Chen, X. W. Wang, *Opt. Lasers Eng.* **2013**, *51*, 134; g) X. T. Zou, N. Wu, Y. Tian, Y. Zhang, J. Fitek, M. Maffeo, C. Niezrecki, J. Chen, X. W. Wang, *Appl. Opt.* **2013**, *52*, 1248; h) J. Chu, J. Beckwith, D. Leonard, C. Paye, R. Greenwald, *Ann. Biomed. Eng.* **2012**, *40*, 203.
[3] T. Gay, *The Physics of Football: Discover the Science of Bone-Crunching Hits, Soaring Field Goals, and Awe-Inspiring Passes*, Harper Collins, New York **2005**.
[4] a) D. K. Cullen, Y. Xu, D. V. Reneer, K. D. Browne, J. W. Geddes, S. Yang, D. H. Smith, *NeuroImage* **2011**, *54*, S37; b) D. K. Cullen, K. D. Browne, Y. A. Xu, S. Adeeb, J. A. Wolf, R. M. McCarron, S. Yang, M. Chavko, D. H. Smith, *J. Neurotrauma* **2011**, *28*, 2307.
[5] J. D. Joannopoulos, R. D. Meade, J. N. Winn, *Photonic Crystals*, Princeton University Press, Princeton, NJ, USA **1995**.
[6] M. Srinivasarao, *Chem. Rev.* **1999**, *99*, 1935.
[7] E. P. Chan, J. J. Walish, A. M. Urbas, E. L. Thomas, *Adv. Mater.* **2013**, *25*, 3934.
[8] S. Y. Lee, S.-H. Kim, H. Hwang, J. Y. Sim, S.-M. Yang, *Adv. Mater.* **2014**, *26*, 2391.
[9] S. H. Park, Y. N. Xia, *Langmuir* **1999**, *15*, 266.
[10] P. Jiang, M. J. McFarland, *J. Am. Chem. Soc.* **2004**, *126*, 13778.
[11] H. Yang, P. Jiang, *Langmuir* **2010**, *26*, 13173.
[12] a) Tarhan II, G. H. Watson, *Phys. Rev. Lett.* **1996**, *76*, 315; b) J. Wijnhoven, W. L. Vos, *Science* **1998**, *281*, 802.
[13] a) C. I. Aguirre, E. Reguera, A. Stein, *Adv. Funct. Mater.* **2010**, *20*, 2565; b) J. P. Ge, J. Goebl, L. He, Z. D. Lu, Y. D. Yin, *Adv. Mater.* **2009**, *21*, 4259.
[14] H. Fudouzi, Y. N. Xia, *Adv. Mater.* **2003**, *15*, 892.
[15] a) K. Lee, S. A. Asher, *J. Am. Chem. Soc.* **2000**, *122*, 9534; b) Y. J. Lee, P. V. Braun, *Adv. Mater.* **2003**, *15*, 563; c) Y. Kang, J. J. Walish, T. Gorishnyy, E. L. Thomas, *Nat. Mater.* **2007**, *6*, 957.
[16] J. H. Kang, J. H. Moon, S. K. Lee, S. G. Park, S. G. Jang, S. Yang, S. M. Yang, *Adv. Mater.* **2008**, *20*, 3061.
[17] a) S. Kubo, Z. Z. Gu, K. Takahashi, A. Fujishima, H. Segawa, O. Sato, *Chem. Mater.* **2005**, *17*, 2298; b) A. Garcia, M. Marquez, T. Cai, R. Rosario, Z. B. Hu, D. Gust, M. Hayes, S. A. Vail, C. D. Park, *Langmuir* **2007**, *23*, 224.
[18] a) A. C. Arsenault, T. J. Clark, G. Von Freymann, L. Cademartiri, R. Sapienza, J. Bertolotti, E. Vekris, S. Wong, V. Kitaev, I. Manners, R. Z. Wang, S. John, D. Wiersma, G. A. Ozin, *Nat. Mater.* **2006**, *5*, 179; b) Y. A. Xu, X. L. Zhu, S. Yang, *ACS Nano* **2009**, *3*, 3251; c) Y. R. Ying, J. Q. Xia, S. H. Foulger, *Appl. Phys. Lett.* **2007**, *90*, 071110; d) E. P. Chan, J. J. Walish, E. L. Thomas, C. M. Stafford, *Adv. Mater.* **2011**, *23*, 4702; e) B. Viel, T. Ruhl, G. P. Hellmann, *Chem. Mater.* **2007**, *19*, 5673; f) M. Kolle, A. Lethbridge, M. Kreysing, J. J. Baumberg, J. Aizenberg, P. Vukusic, *Adv. Mater.* **2013**, *25*, 2239; g) M. A. Haque, G. Kamita, T. Kurokawa, K. Tsujii, J. P. Gong, *Adv. Mater.* **2010**, *22*, 5110.
[19] Y. Zhang, C.-T. Lin, S. Yang, *Small* **2010**, *6*, 768.
[20] E. Kim, Y. Xia, G. M. Whitesides, *J. Am. Chem. Soc.* **1996**, *118*, 5722.
[21] K. Y. Suh, Y. S. Kim, H. H. Lee, *Adv. Mater.* **2001**, *13*, 1386.
[22] R. Feng, R. J. Farris, *J. Micromech. Microeng.* **2003**, *13*, 80.
[23] J. H. Jang, C. K. Ullal, T. Y. Choi, M. C. Lemieux, V. V. Tsukruk, E. L. Thomas, *Adv. Mater.* **2006**, *18*, 2123.
[24] L. F. Wang, M. C. Boyce, C. Y. Wen, E. L. Thomas, *Adv. Funct. Mater.* **2009**, *19*, 1343.
[25] H. Fudouzi, T. Sawada, *Langmuir* **2006**, *22*, 1365.

[26] J. Li, Y. Cho, I.-S. Choi, S. Yang, *Adv. Funct. Mater.* **2013**, *24*, 2361.
[27] S. P. Broglio, J. J. Sosnoff, S. Shin, X. M. He, C. Alcaraz, J. Zimmerman, *J. Athl. Train.* **2009**, *44*, 342.
[28] S. Singamaneni, K. Bertoldi, S. Chang, J. H. Jang, E. L. Thomas, M. C. Boyce, V. V. Tsukruk, *ACS Appl. Mater. Interfaces* **2009**, *1*, 42.
[29] J. Li, J. Shim, J. Deng, J. T. B. Overvelde, X. Zhu, K. Bertoldi, S. Yang, *Soft Matter* **2012**, *8*, 10322.
[30] J. H. Jang, C. K. Ullal, T. Choi, M. C. Lemieux, V. V. Tsukruk, E. L. Thomas, *Adv. Mater.* **2006**, *18*, 2123.
[31] K. D. Hartlen, A. P. T. Athanasopoulos, V. Kitaev, *Langmuir* **2008**, *24*, 1714.
[32] W. Stöber, A. Fink, *J. Colloid Interface Sci.* **1968**, *26*, 62.